JACS
JOURNAL OF THE AMERICAN CHEMICAL SOCIETY

ARTICLE

pubs.acs.org/JACS

Defects in Doped $LaGaO_3$ Anionic Conductors: Linking NMR Spectral Features, Local Environments, and Defect Thermodynamics

Frédéric Blanc,[†,‡] Derek S. Middlemiss,[†,‡] Zhehong Gan,[§] and Clare P. Grey*[,†,‡]

[†]Department of Chemistry, State University of New York, Stony Brook, New York 11790-3400, United States

[‡]Department of Chemistry, University of Cambridge, Lensfield Road, Cambridge CB2 1EW, U.K.

[§]National High Magnetic Field Laboratory, 1800 East Paul Dirac Drive, Tallahassee, Florida 32310-3706, United States

Supporting Information

ABSTRACT: Doped lanthanum gallate perovskites ($LaGaO_3$) constitute some of the most promising electrolyte materials for solid oxide fuel cells operating in the intermediate temperature regime. Here, an approach combining experimental multinuclear NMR spectroscopy with density functional theory total energy and GIPAW NMR calculations yields a comprehensive understanding of the structural and defect chemistries of Sr- and Mg-doped $LaGaO_3$ anionic conductors. The DFT energetics demonstrate that Ga−V_O−Ga (V_O = oxygen vacancy) environments are favored (vs Ga−V_O−Mg, Mg−V_O−Mg and Mg−O−Mg−V_O−Ga) across a range $y = 0.0625$, 0.125, and 0.25 of fractional Mg contents in $LaGa_{1-y}Mg_yO_{3-y/2}$. The results are interpreted in terms of doping and mean phase formation energies (relative to binary oxides) and are compared with previous calculations and experimental calorimetry data. Experimental multinuclear NMR data reveal that while Mg sites remain six-fold coordinated across the range of phase stoichiometries, albeit with significant structural disorder, a stoichiometry−dependent minority of the Ga sites resonate at a shift consistent with Ga^V coordination, demonstrating that O vacancies preferentially locate in the first anion coordination shell of Ga. The strong Mg−V_O binding inferred by previous studies is not observed here. The ^{17}O NMR spectra reveal distinct resonances that can be assigned by using the GIPAW NMR calculations to anions occupying equatorial and axial positions with respect to the Ga^V−V_O axis. The disparate shifts displayed by these sites are due to the nature and extent of the structural distortions caused by the O vacancies.

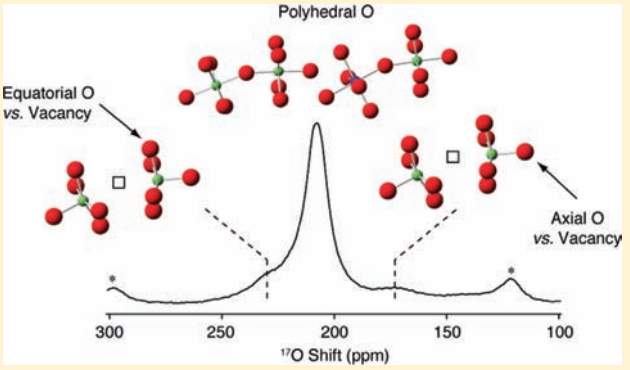

1. INTRODUCTION

Anionic conductors find widespread use in a range of important electrochemical technologies such as oxygen sensors, oxygen separation membranes, and solid oxide fuel cells (SOFCs). While materials displaying high anionic conductivity, such as yttria-stabilized zirconia (YSZ) and substituted CeO_2, have found use in high temperature (800−1000 °C) SOFC applications, there is considerable interest in developing stable electrolytes suitable for deployment at lower temperatures in the so-called intermediate regime (T < 800 °C). Perovskite-type oxides (ABO_3), wherein the 12-fold coordinated A^{XII} cations occupy the centers of cubes composed of octahedrally coordinated B^{VI} cations, are often proposed as candidate materials, due to their high tolerance for substitutional doping upon both the A and B sublattices. This is an important characteristic, given that divalent and trivalent substitution of majority trivalent and tetravalent cations, respectively, are typically compensated by an increase in the concentration of charge-carrying O vacancies (denoted as V_O hereafter), with concomitant improvement in anionic conductivity (at least for low doping levels). A range of perovskite-type oxides have been considered for such applications, including doped $LaMO_3$ (M = Ga, Al, Sc, In, and Ln),[1−9] but the promisingly high conductivities obtained for doped $LaGaO_3$ phases (Figure 1) have been and continue to be of particular interest. A variety of doping schemes have been investigated, including substitution of Ca^{2+}, Sr^{2+}, and Ba^{2+} for La^{3+} and Al^{3+}, In^{3+}, and Mg^{2+} for Ga^{3+}, the dopants often being simultaneously introduced on both cation sublattices.[1−6,10] Systematic studies indicate that Sr- and Mg-doped $LaGaO_3$, the material studied in detail here, constitute one of the most highly anion conductive family of compounds,[1,2] both dopant species introducing O vacancies.

While conventional diffraction-based techniques are routinely applied to the structural characterization of materials, they provide little insight into the local environments experienced by defect species. The mobility of constituent species may be inferred, for example, from variations in thermal parameters or from spread in the electron or nuclear density distribution, but it is clear that this represents a lattice average and does not necessarily reflect the mobility in a region close to a specific defect or dopant.

Received: June 9, 2011
Published: September 14, 2011

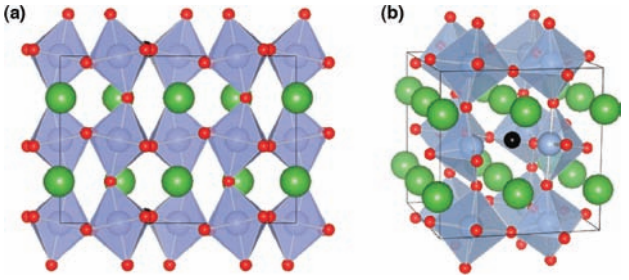

Figure 1. (a) Orthorhombic structure of pure $LaGaO_3$ showing the degree of GaO_6 octahedral tilting (red, purple, and green spheres denote O, Ga, and La sites, respectively). (b) Schematic of an oxygen vacancy, V_O, (black sphere) in $LaGaO_3$, forming two neighboring square pyramidal GaO_5 environments.

However, recent work in our group[11−16] and by other investigators[17−20] demonstrates that local environments and dynamics in oxygen-conducting phases may be readily obtained from an approach combining solid-state nuclear magnetic resonance (NMR) spectroscopy with first principles quantum mechanical simulations.[21,22] NMR offers the key advantage in that it affords multiple perspectives into the environments and processes (e.g., mobility) of interest, via experiments targeting a range of nuclei. However, the interpretation of the spectra obtained is often difficult, particularly within complex phases for which representative model compounds may not be available. Solid-state calculations of NMR parameters within the gauge, including the projector augmented wave (GIPAW) approach,[23,24] are of great assistance in this regard,[14,15,25−39] providing shielding and electric field gradient tensors for sites of interest. Here we use this approach, and report a combined experimental and theoretical study of the defect chemistry of Sr- and Mg-doped $LaGaO_3$ on the basis of multinuclear NMR of ^{71}Ga, ^{25}Mg, and ^{17}O sites,[13] which supports a very recent detailed experimental study carried out on these systems based upon a static multinuclear NMR approach.[40] We focus in particular on $La_{1-x}Sr_xGa_{1-y}Mg_yO_{3-(x+y)2}$ (experimental x, $y \leq 0.2$; theory $x = 0$, $y \leq 0.25$) stoichiometries, motivated by the promising performance of these phases as SOFC electrolytes operating above 700 °C.[1,2,4,40]

Direct comprehensive NMR studies of defects in inorganic phases are generally challenging,[11,14,16,40−43] often due to the fact that the substituents and charge balancing species are present at low concentrations, occasionally falling below the level of native defects and impurities. The assignment difficulties mentioned above become even more acute in defective and doped phases bearing atypical local environments and coordinations. Here, however, we demonstrate that an approach combining previously determined experimental correlations linking isotropic chemical shifts with coordination number[21,44−47] and DFT-based total energy and NMR calculations overcomes these difficulties. We show that the compensatory O vacancies in Sr- and Mg-doped $LaGaO_3$ preferentially locate between Ga^{3+} ions, helping to resolve the debate in the literature concerning the location of the defects.[5,40,48−50] Our observations contradict previous findings and interpretations obtained on the basis of conductivity measurements[5,50] and interatomic potentials calculations[48,49] but are in agreement with recently reported NMR studies.[40] Moreover, the DFT calculations allow new features observed in the ^{17}O spectra of the doped phases to be assigned, demonstrating for the first time the high sensitivity of anion NMR to local lattice distortions introduced by nearby vacancies.

2. EXPERIMENTAL AND THEORETICAL METHODS

2.1. Synthesis. Undoped and Sr- and Mg-doped $LaGaO_3$ samples were prepared via the solid-state reaction route described previously.[2,51] Calculated amounts of La_2O_3 (Aldrich, 99.99%, heated overnight at 1000 °C under air), Ga_2O_3 (Aldrich, 99.99%, used as received), $SrCO_3$ (Aldrich, 99.99%, used as received), and MgO (Aldrich, 99.99%, heated overnight at 1000 °C) were mixed in a mortar and pestle, pressed isostatically into a disk, and then sintered at 1500 °C for 6−12 h. The powders were then ground, repressed, and resintered at 1500 °C for 6 h.

Magnesium ^{25}Mg enrichments followed the same synthesis route described above, using 98% ^{25}Mg-enriched MgO (Cambridge Isotope Laboratories, heated overnight at 1000 °C). Oxygen ^{17}O enrichment was performed by heating the samples twice in a flame-sealed Pyrex tube under 50% ^{17}O-enriched $^{17}O_2$ gas (Isotec, used as received) at 600 °C in a tube furnace for 24 h. The phases present in all the enriched and nonenriched samples were identified by Cr Kα powder X-ray diffraction measurements using a Rigaku X-ray diffractometer (Figure S1).

2.2. Solid-State NMR Spectroscopy. Static ^{71}Ga NMR experiments were performed on a 8.5 T Varian Chemagnetics Infinity Plus 360 MHz spectrometer using a Chemagnetics 4 mm HX probe, a 9.4 T Bruker Avance 400 MHz spectrometer using a Bruker 4 mm HX probe, a 14.1 T Bruker Avance 600 MHz spectrometer using a Bruker triple resonance 4 mm HXY probe (in double resonance mode), and finally a 20 T Bruker Avance III 850 MHz spectrometer using a Bruker triple resonance 3.2 mm HXY (in double resonance mode). Spectra were recorded using a static full echo sequence with a selective $\pi/2$ pulse length of 1.25 μs at a radio frequency (rf) field amplitude of 100 kHz at 8.45, 9.4, and 14.1 T, and of 1.0 μs at a rf field amplitude of 125 kHz at 20 T. A recycle delay of 0.2 s, sufficient to obtain quantitative data, was used for all static ^{71}Ga experiments.

Low-field MAS ^{25}Mg NMR experiments were carried out on an 11.7 T Varian Infinity Plus 500 MHz spectrometer equipped with a Chemagnetics 4 mm HX probe. Rotor synchronized Hahn echo experiments were carried out with one rotor period of evolution/refocusing to avoid probe ring down. A selective short pulse length $\pi/6 = 0.8$ μs at a rf field of 35 kHz was used at a recycle delay of 0.5 s. High-field MAS ^{25}Mg NMR spectra were obtained at 19.6 T on a Bruker DRX 830 MHz spectrometer at the National High Magnetic Field Laboratory, Tallahassee, Florida, USA, using a home-built 4 mm single channel probe. Single-pulse experiments were performed with a selective $\pi/2$ pulse of 1.0 μs at a rf field of 90 kHz. Two-dimensional (2D) triple-quantum MAS experiments were performed using a shifted echo pulse sequence and the soft-pulse-added-mixing (SPAM).[52−54] Twenty t_1 increments of 10200 scans were co-added. Hard and soft pulses were performed at rf fields of 90 and 20 kHz, respectively. Fully relaxed spectra were recorded with a recycle delay set to 0.3 s. All experiments were performed under MAS of 10 kHz.

Low-field MAS ^{17}O NMR experiments were carried out on the 11.7 T Infinity Plus spectrometer, now with a Chemagnetics 4 mm HXY probe, the Y channel being tuned to ^{17}O. The samples were center packed in a 4 mm rotor and rotor synchronized Hahn echo experiments carried out with one rotor period. A short pulse length $\pi/6 = 0.55$ μs at a rf field of 50 kHz, a recycle delay of 0.5 s, and a spinning frequency, ω_r, of 15 kHz were used. High-field MAS ^{17}O NMR were obtained on the 19.6 T Bruker DRX spectrometer again with a home-built 4 mm single channel probe. Single pulse experiments were performed with a pulse length $\pi/2 = 1.0$ μs at a rf field of 120 kHz. Two-dimensional triple-quantum MAS experiments were performed using a shifted echo pulse sequence and the soft-pulse-added-mixing (SPAM) technique.[52−54] Sixteen t_1 increments of 5000 scans were co-added. Hard and soft pulses were performed at rf fields of 120 and 20 kHz, respectively. Recycle delays of 0.3 s and ω_r of 10 kHz were used.

The ^{17}O, ^{25}Mg, and ^{71}Ga chemical shifts were externally referenced to water, to a 1 M solution of $MgCl_2$ (or $Mg(NO_3)_2$) in water, and to a 1 M solution of $Ga(NO_3)_3$ in water, respectively, all at 0.0 ppm.

NMR data were processed using the MatNMR package[55] implemented within MatLab. Simulations were performed using MatNMR[55] and/or SIMPSON[56] using standard numerical techniques.[57] Simulations of the distribution of ^{25}Mg quadrupolar interactions were performed using a general Gaussian isotropic model[58−60] (originally derived from the Czjzek distribution,[61] see Supporting Information for more details) as implemented in commercial software.[62−64]

2.3. Electronic Structure Calculations. First principles, periodic solid-state DFT calculations were performed within the CASTEP code, providing total energies, optimized structures and NMR parameters for all configurations considered. The magnetic shielding tensor (σ_s) at each site in the cell was obtained within the GIPAW approach. The reference shielding (σ_{ref}), required to convert from the absolute shielding provided by the code to the isotropic chemical shift (δ_{iso}) relevant to experiment, is obtained via an expression of the general form $\delta_{iso} = \sigma_{ref} + m_{ref}\sigma_{iso}$, where m_{ref} is a gradient normally lying close to or assumed equal to −1. The shielding reference data for ^{17}O (σ_{ref} = 223.70 ppm, m_{ref} = −0.888, rms error =12.1 ppm) and ^{71}Ga sites (σ_{ref} = 1502.63 ppm, m_{ref} = −0.867, rms error = 7.3 ppm) were taken from our recent study of a wide range of perovskites and Ga-bearing phases,[15] and, for ^{25}Mg sites (σ_{ref} = 538.83 ppm, m_{ref} = −0.953, standard deviation = 11.9 ppm), from the study of a wide range of Mg oxyanions by Cahill et al.[27] The isotropic shielding is defined as $\sigma_{iso} = 1/3(\sigma_{xx}+\sigma_{yy}+\sigma_{zz})$, where σ_{xx}, σ_{yy}, and σ_{zz} are the principal components of the shielding tensor at each nuclear position, oriented such that $|\sigma_{zz}-\sigma_{iso}| \geq |\sigma_{xx}-\sigma_{iso}| \geq |\sigma_{yy}-\sigma_{iso}|$. Shielding anisotropies and asymmetries are defined as $\sigma_{aniso} = \sigma_{zz}-1/2(\sigma_{xx}+\sigma_{yy})$, and $\eta_{cs} = (\sigma_{yy}-\sigma_{xx})/(\sigma_{zz}-\sigma_{iso})$, respectively. The quadrupolar coupling constants, $C_Q = eQV_{zz}/h$, and asymmetry parameters, $\eta_Q = (V_{xx}-V_{yy})/V_{zz}$, are obtained directly from the principal components $|V_{zz}| \geq |V_{yy}| \geq |V_{xx}|$ of the electric field gradient tensor computed at each site[65] where Q is the appropriate nuclear quadrupole moment provided by Pyykkö.[66]

In validation of the methods outlined above, we note that our previous calculations included a range of bridging oxygen environments, together with Ga^{VI}, Ga^{IV} sites and the rare Ga^{V} environment occurring in the $LaGaGe_2O_7$ phase, the computed shifts of all of which were found to be in good agreement with experiment.[15,46]

The thermodynamics of O vacancy-compensated Mg-doping were assessed for a range of Mg/V_O configurations in supercell stoichiometries $La_{32}Ga_{30}Mg_2O_{95}$ (159 atoms, y = 0.0625, nine configurations considered: four Ga−V_O−Ga, four Mg−V_O−Ga, and one Mg−V_O−Mg), $La_{16}Ga_{14}Mg_2O_{47}$ (79 atoms, y = 0.125, sixteen configurations considered: eight Ga−V_O−Ga, seven Mg−V_O−Ga, and one Mg−V_O−Mg) and $La_8Ga_6Mg_2O_{23}$ (39 atoms, y = 0.25, nine configurations considered: four Ga−V_O−Ga, four Mg−V_O−Ga, and one Mg−V_O−Mg). All configurations were fully geometry optimized (both cell and atomic positions) without symmetry constraints, employing a plane wave kinetic energy cutoff of E_C = 40 Ry, Monkhorst−Pack (MP) **k**-space sampling meshes with dimensions 2×2×2 (159 atom supercells), 2×2×2 (79 atom supercells), and 4×4×4 (39 atom supercells), and total energy, force, displacement, and stress convergence tolerances of 1×10^{-6} eV, 5×10^{-3} eV Å^{-1}, 1×10^{-4} Å and 5×10^{-3} GPa, respectively. Electron exchange and correlation were treated within the Perdew, Burke, and Ernzerhof (PBE) GGA-type functional.[67] Given the high computational effort involved, NMR calculations were pursued only for the sixteen $La_{16}Ga_{14}Mg_2O_{47}$ configurations using the respective optimized geometries, a 2×2×2 MP mesh and an increased cutoff E_C = 50 Ry. The numerical conditions adopted yield convergence in computed isotropic shieldings to better than 1 ppm for all species. Calculations of the various thermodynamic parameters take as reference the total energies of face-centered cubic MgO, hexagonal La_2O_3, monoclinic β-Ga_2O_3, orthorhombic $LaGaO_3$, and spinel $MgGa_2O_4$, all of which were obtained from full geometry optimizations using convergence tolerances identical to those above, with cutoff E_C = 40 Ry and well-converged MP meshes 14×14×14, 10×10×6, 12×12×6, 7×7×5, and 7×7×7, respectively.

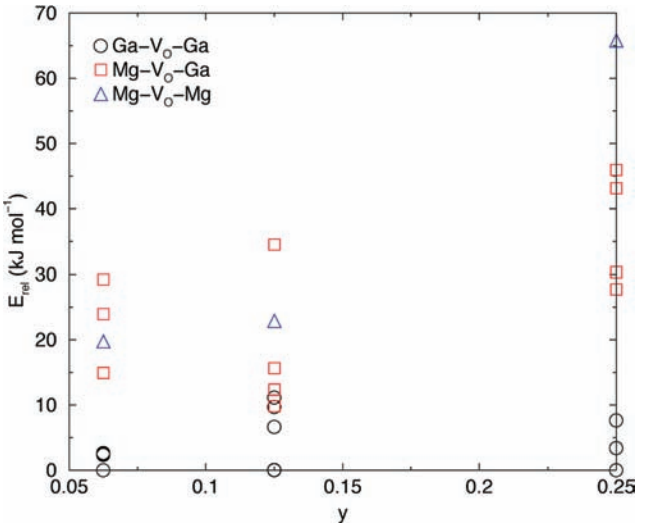

Figure 2. Total energies of the $LaGa_{1-y}Mg_yO_{3-(y/2)}$ supercells (kJ·mol^{-1}) for all configurations considered. The energy E_{rel} of each configuration relative to the total energy of the most stable configuration at each fractional Mg content y is plotted. The configurations are split into three classes, depending upon the cations neighboring the O vacancy (V_O) center.

3. RESULTS AND DISCUSSION

3.1. DFT Energetics. Prior to calculations of NMR parameters, the phase energetics of Mg-doped $LaGaO_3$ are examined. The 34 configurations described above for y = 0.0625, 0.125, and 0.25 (classed as Ga−V_O−Ga, Mg−V_O−Ga, or Mg−V_O−Mg type, depending upon the cation species immediately adjacent to the O vacancy) were fully geometry optimized and ranked in terms of calculated total energies. The supercells of the $LaGaO_3$ structure used in the calculations contained between 39 and 159 atoms, the larger sizes being required to investigate the lower substitution levels. As an important preliminary, we tested for the need to include spin polarization, by obtaining the total energies of electronic states bearing one and two unpaired electrons for the lowest energy y = 0.125 Ga−V_O−Ga and Mg−V_O−Ga configurations found above. The magnetic solutions emerge at energies ranging from 301 to 332 kJ·mol^{-1} above the respective diamagnetic ground states, sufficiently high that spin polarization may reasonably be neglected in all subsequent calculations.

The supercell total energies are plotted relative to the most stable configuration found for each fractional Mg content in Figure 2. It is clear that Ga−V_O−Ga geometries are energetically favored across the range of fractional Mg contents. This is an interesting finding, given that previous interatomic potentials calculations[49] have suggested a strong preference for vacancies to occupy sites immediately neighboring Mg_{Ga}' dopants, with substantial associated binding energies of −87 kJ·mol^{-1}·defect^{-1} for Mg−V_O pairs, and −118 kJ·mol^{-1}·defect^{-1} for Mg−V_O−Mg trimers. An earlier study, again using interatomic potentials, reported a near identical Mg−V_O pair binding energy of −85 kJ·mol^{-1}·defect^{-1}.[48] Subsequent variable temperature (T) conductivity measurements have been interpreted on this basis, the non-Arrhenius behavior evident in log $\sigma(T)$ vs $1/T$ plots being attributed to nearly complete trapping of vacancies at low temperature and nearly completely unbound vacancies at high temperature, the anion motion in the latter case being

Table 1. Variation in Computed Thermodynamic Parameters of the $LaGa_{1-y}Mg_yO_{3-(y/2)}$ Phases with Fractional Mg Content, y[a]

y	E^{A}_{defect} / kJ·mol^{-1}	E^{B}_{defect} / kJ·mol^{-1}	E^{C}_{defect} / kJ·mol^{-1}	E_{form} / kJ·mol^{-1}
0				−27
0.0625	86	73	111	−22
	(σ_{sd} = 5.8)	(σ_{sd} = 5.8)	(σ_{sd} = 5.8)	(σ_{sd} = 0.34)
0.1250	85	72	109	−16
	(σ_{sd} = 4.8)	(σ_{sd} = 4.8)	(σ_{sd} = 4.8)	(σ_{sd} = 0.57)
0.2500	88	75	112	−6
	(σ_{sd} = 11.6)	(σ_{sd} = 11.6)	(σ_{sd} = 11.6)	(σ_{sd} = 2.94)
Previous studies	~580,[48]	~100[69]	~135[69]	**y = 0:** −19.3[69]
				~−53,[72] −50.86,[70]
	~190[49]			−32[71]
				y = 0.09: −40.4,[72]
				y = 0.18: −27.7[72]

[a] The mean defect (A, B, and C) and phase formation energies (kJ·mol^{-1}) are as defined in the text, where mean values and standard deviations (σ_{sd}) have been computed over all configurations at a given y value.

hindered only by the normal diffusion barriers.[50] However, the present DFT results do not support this, finding no tendency toward the formation of $Mg-V_O$ bound pairs (for either first or second nearest neighbor $Mg-V_O$ pairs) at fractional Mg contents relevant to electrolyte applications. We suggest that the non-Arrhenius character of the log σ vs $1/T$ plot, in $LaGaO_3$-derived phases at least, must instead be related to temperature-induced variations in the crystal structure, and possibly to the progressive increase in the mean area of the O diffusion AAB-bottleneck with both temperature and dopant concentration observed in a recent neutron diffraction study of a range of doped $LaGaO_3$ phases.[68]

Examining the data for the more numerous $y = 0.125$ configurations in detail, it is found that the relative total energies for the eight $Ga-V_O-Ga$ configurations considered fall in the range 0 (ground state) to +11 kJ·mol^{-1}; the seven $Mg-V_O-Ga$ configurations, +10 to +16 kJ·mol^{-1}; and the Mg-clustered $Mg-V_O-Mg$ and $Mg-O-Mg-V_O-Ga$ (i.e., a vacancy adjacent to a $Mg-O-Mg$ linkage), at +23 and +35 kJ·mol^{-1}, respectively. We have not examined all possible Mg/V_O arrangements in the 79-atom supercell and therefore cannot comment on the configurational entropies of the lowest-energy states. However, the thermal energy k_BT at a typical synthesis temperature of 1800 K amounts to 15 kJ·mol^{-1}, rendering it likely that a significant fraction of higher-energy $Mg-V_O-Ga$ environments will be present in the as-synthesized $y = 0.125$ phase. This is likely also true in the $y = 0.0625$ phase, where the energy gap separating the most stable $Ga-V_O-Ga$ and $Mg-V_O-Ga$ configurations amounts to only 15 kJ·mol^{-1}. The corresponding energy gap at $y = 0.25$ is, however, significantly broader at 28 kJ·mol^{-1}. Again, we emphasize that this analysis must be regarded as tentative, given the lack of a full determination of the energies of all possible Mg/V_O arrangements in each supercell.

As a further test of the present approach, we compute the energy of formation of the $Mg_{Ga}' + 1/2\ V_O^{\bullet\bullet}$ defect with respect to thermodynamical phase equilibria A = ($LaGaO_3-MgO-\beta$-Ga_2O_3), B = ($LaGaO_3-MgO-MgGa_2O_4$), and C = ($LaGaO_3-\beta$-$Ga_2O_3-MgGa_2O_4$), with energies defined as

$$E^{A}_{defect}(y) = \frac{1}{2}E(La_{2/y}Mg_2Ga_{(2/y)-2}O_{(6/y)-1}) + \frac{1}{2}E(\beta - Ga_2O_3) - E(MgO) - \frac{1}{2}E(La_{2/y}Ga_{2/y}O_{6/y}) \quad (1)$$

$$E^{B}_{defect}(y) = \frac{1}{2}E(La_{2/y}Mg_2Ga_{(2/y)-2}O_{(6/y)-1}) + \frac{1}{2}E(MgGa_2O_4) - \frac{3}{2}E(MgO) - \frac{1}{2}E(La_{2/y}Ga_{2/y}O_{6/y}) \quad (2)$$

$$E^{C}_{defect}(y) = \frac{1}{2}E(La_{2/y}Mg_2Ga_{(2/y)-2}O_{(6/y)-1}) + \frac{3}{2}E(\beta - Ga_2O_3) - E(MgGa_2O_4) - \frac{1}{2}E(La_{2/y}Ga_{2/y}O_{6/y}) \quad (3)$$

The equilibria were chosen to permit comparisons with the defect energies derived by the previous theoretical studies.[48,49,69] We also obtain the energies of formation of the $LaGa_{1-y}Mg_yO_{3-(y/2)}$ ($0 \le y \le 0.25$) phases relative to the La_2O_3 and Ga_2O_3 sesquioxides and MgO monoxide, the energy being defined as

$$E_{form}(y) = E(LaGa_{1-y}Mg_yO_{3-(y/2)}) - \frac{1}{2}E(La_2O_3) - \frac{1}{2}(1-y)E(\beta - Ga_2O_3) - yE(MgO) \quad (4)$$

where, again, we seek to make contact with previous theoretical[69] and experimental studies.[70−72] The computed thermodynamic parameters, standard deviations, and comparable previous experimental and theoretical values are presented in Table 1.

Seeking contact with previous interatomic potential simulations,[48,49] we examine the mean $E^{A}_{defect}(y)$ (defect formation in equilibrium with $LaGaO_3$, MgO, and β-Ga_2O_3) energies. A consistent mean value of approximately 86 kJ·mol^{-1} emerges across the range of stoichiometries, lying significantly below the values of approximately 580[48] and 190 kJ·mol^{-1} [49] obtained from the interatomic potential calculations. While the earlier calculations derived formation energies for formally isolated $MgGa'$ and $V_O^{\bullet\bullet}$ centers, the apparent insensitivity of the present $E^{A}_{defect}(y)$ values (in comparison to the large spread of energies for the different configurations) to fractional Mg content, over the range investigated, suggests that the present and previous values may be directly compared. The large differences in formation energy must therefore come from the disparate total energy methods used, the DFT-based approach pursued here including dopant-induced variations in electronic structure and elastic effects commensurate with the supercell sizes used.

dx.doi.org/10.1021/ja2053557 |J. Am. Chem. Soc. 2011, 133, 17662–17672

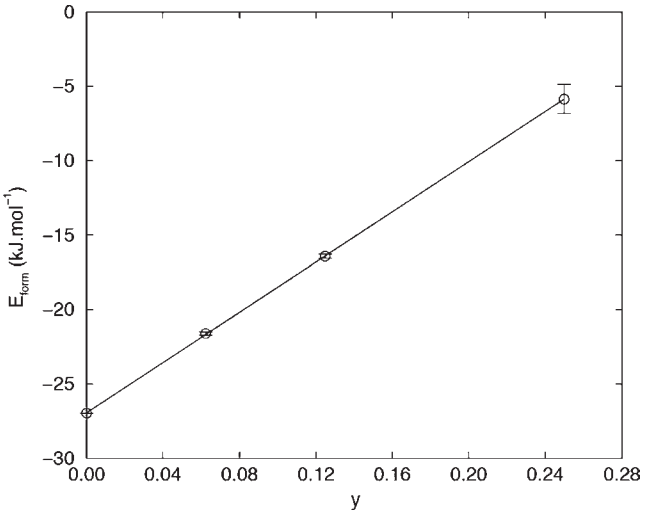

Figure 3. Mean formation energies ($kJ \cdot mol^{-1}$) of the $LaGa_{1-y}Mg_yO_{3-(y/2)}$ phases relative to the MgO, La_2O_3, and β-Ga_2O_3 oxides, plotted as a function of the oxygen deficiency. Error bars are obtained from the standard deviations computed across all configurations at a given y value. The solid line denotes a linear fit with gradient 84.3 ± 0.3 $kJ \cdot mol^{-1}$ and intercept −26.93 ± 0.04 $kJ \cdot mol^{-1}$.

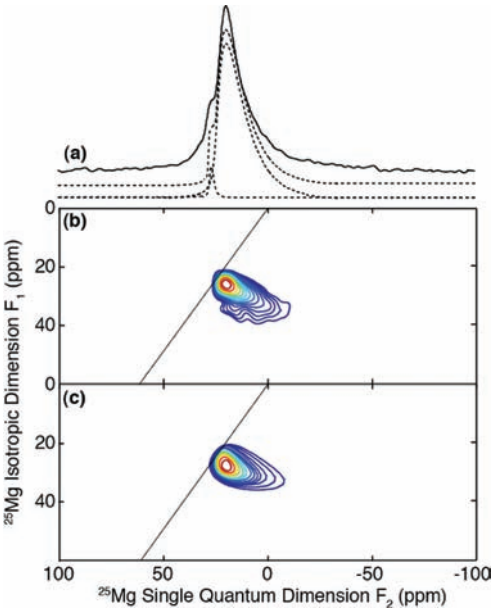

Figure 4. ^{25}Mg MAS and MQMAS spectra of ^{25}Mg-enriched $La_{0.8}Sr_{0.2}Ga_{0.8}Mg_{0.2}O_{2.8}$. (a) ^{25}Mg MAS spectrum at 19.6 T. The best-fit simulations (dashed lines) corresponding to the PDF of the quadrupolar parameters derived from a Gaussian isotropic model are shown below the experimental spectra (Tables 2 and S1). (b) Two-dimensional sheared ^{25}Mg 3Q MAS spectrum at 19.6 T. (c) Simulation of the ^{25}Mg 3Q MAS spectrum at 19.6 T using the parameters given in Tables 2 and S1. The diagonal line represents the isotropic correlation line.

Contact with an earlier DFT study[69] of Mg-doping comes via an examination of the mean E^{B}_{defect} (y) (defect formation in equilibrium with $LaGaO_3$, MgO, and $MgGa_2O_4$) and E^{C}_{defect} (y) (defect formation in equilibrium with $LaGaO_3$, β-Ga_2O_3, and $MgGa_2O_4$) energies. We again observe a high degree of insensitivity to fractional Mg content, yielding mean values across all stoichiometries of 74 and 111 $kJ \cdot mol^{-1}$, respectively. The previous DFT calculations provided values of approximately 100 and 135 $kJ \cdot mol^{-1}$, respectively, in satisfactory agreement with the present results when it is considered that the previous study considered isolated Mg_{Ga}' and $V_O^{\bullet\bullet}$ centers in charge−neutralized supercells (including associated estimated corrections of formation energies) and limited structural relaxation to a spherical volume of radius 3.2 Å centered on the defect site.[69]

Finally, the mean formation energies of $LaGa_{1-y}Mg_yO_{3-(y/2)}$ relative to the oxides are presented in Table 1 and shown graphically in Figure 3. First, the computed formation energy of the pure phase at −27 $kJ \cdot mol^{-1}$ is relatively close to the value −19 $kJ \cdot mol^{-1}$ obtained from the DFT calculations of Kuwabara and Tanaka[69] and lies 5 to 26 $kJ \cdot mol^{-1}$ higher than the comparable experimental values. Our accuracy here is comparable to a recent DFT study of a broader range of perovskite-related phases, wherein the computed formation energies from binary oxides yielded a mean absolute error of 14 $kJ \cdot mol^{-1}$ relative to experimental values.[73] The calculated progressive destabilization of the doped lattice with increasing oxygen deficiency is in broad agreement with the calorimetry results of Cheng and Navrotsky (Figure 2),[72] albeit that the enthalpy of vacancy formation obtained in the experimental study as $d\Delta H_{form}/dy$ =138 ± 19 $kJ \cdot mol^{-1}$ (298 K) is significantly underestimated here at 84 ± 1 $kJ \cdot mol^{-1}$. In addition to the inherent limitations of DFT-based thermodynamics in perovskites discussed by Calle−Vallejo et al.[73] and referenced above, some of this discrepancy is likely due to the neglect of both zero point and finite temperature vibrational contributions in the present approach.

Summarizing the theoretical energetics, our key finding is that the strong Mg−V_O binding observed within the previous interatomic potentials simulations[48,49] is not supported by the present DFT calculations. Instead, a weak energetic preference for Ga−V_O−Ga configurations is found across the range of stoichiometries. The higher-energy Mg−V_O−Ga configurations in the y = 0.0625 and 0.125 phases are, however, likely to be accessible at the temperatures used to synthesize these materials. The computed $Mg_{Ga}' + {}^1/_2V_O^{\bullet\bullet}$ defect formation energies within a range of phase equilibria are in reasonable agreement with previous DFT results[69] but significantly underestimate the values obtained from earlier interatomic potentials calculations.[48,49] Finally, the computed progressive destabilization of $LaGa_{1-y}Mg_yO_{3-y/2}$ with respect to increasing Mg content is in broad qualitative agreement with earlier calorimetric measurements,[72] albeit that the DFT results significantly underestimate the enthalpy of vacancy formation.

3.2. Nuclear Magnetic Resonance. *3.2.1. ^{25}Mg.* Representative ^{25}Mg NMR spectra of ^{25}Mg-enriched $La_{0.8}Sr_{0.2}Ga_{0.8}Mg_{0.2}O_{2.8}$ obtained at magnetic field strength of 19.6 T is shown in Figure 4a, while similar spectra, collected at various fields, for the series $La_{1-x}Sr_xGa_{1-y}Mg_yO_{3-(x+y)/2}$ (x,y = 0.1−0.2) are shown in Figures S4−S7. All samples give rise to an asymmetrically broadened peak at around 24−20 ppm with a tail to low frequency due to Mg ions substituted on the perovskite B-site sublattice.[1,2] The broadening arises from the second-order quadrupolar interaction, which, for deviations in the site symmetry from either cubic, octahedral or tetrahedral symmetry, gives rises to distinctive spectral lineshapes. The 'tail' is caused by a distribution of quadrupolar couplings,[74] and is therefore a strong indicator of the presence of significant structural disorder (see below). A weaker sharp resonance is also observed at 26 ppm, which corresponds to Mg^{2+} ions located on the octahedral sites of unreacted ^{25}MgO starting material (not observed by XRD, Figure S2). The residual second-order

Table 2. Experimental (x,y = 0.1−0.2) and Calculated (y = 0.125) ^{25}Mg, ^{71}Ga, and ^{17}O NMR Parameters for $La_{1-x}Sr_xGa_{1-y}Mg_yO_{3-(x+y)/2}$ Phases[a]

site	coordination	δ_{iso} / ppm	C_Q / MHz	η_Q
Mg	VI	**21(2**[b]**)**	**1−2**[c]	−[d]
		16(σ_{sd} = 2)	3.0(σ_{sd} = 1.2)	0.55(σ_{sd} = 0.33)
	V		**n.o.**[e]	
		38(σ_{sd} = 1)	7.7(σ_{sd} = 1.0)	0.14(σ_{sd} = 0.03)
Ga	VI	**58(4)**	**1.4(4)**	**0.0(3)**
		55(σ_{sd} = 8)	5.0(σ_{sd} = 2.7)	0.53(σ_{sd} = 0.25)
	V	**72(22)**	**8.3(24)**	**0.4(5)**
		150(σ_{sd} = 8)	10.1(σ_{sd} = 2.0)	0.46(σ_{sd} = 0.27)
O[f]	$M^{VI}-O_{ax}-M^{V}$	**182(9)**	**6(2)**	**0.5(5)**
		186(σ_{sd} = 15)	3.1(σ_{sd} = 1.0)	0.32(σ_{sd} = 24)
	$M^{VI}-O-M^{VI}$	**223(3)**	**3.3(3)**	**0.3(2)**
		221(σ_{sd} = 7)	3.4(σ_{sd} = 0.7)	0.26(σ_{sd} = 0.14)
	$M^{VI}-O_{eq}-M^{V}$	**244(20)**	**3.7(7)**	**0.6(6)**
		247(σ_{sd} = 8)	3.6(σ_{sd} = 0.9)	0.43(σ_{sd} = 0.14)

[a] Experimental and calculated values in bold and plain text, respectively. (M = Ga or Mg) ^{25}Mg and ^{17}O experimental values were determined from the MQMAS spectra at 19.6 T, while the ^{71}Ga values were extracted from fits of the static spectra at various magnetic field strengths. Parameters only for the sites in the $La_{1-x}Sr_xGa_{1-y}Mg_yO_{3-(x+y)/2}$ phases are presented in Table 1. The ^{71}Ga NMR parameters of the $LaSrGa_3O_7$ impurity are: δ_{iso} = 227(14) ppm, C_Q = 2.8(19) MHz, and η_Q = 0.2(6). Detailed experimental (Tables S1, S3 and S5) and calculated (Tables S2, S4, and S6) data are given in the Supporting Information file. Theoretical shielding (σ) references in the form $\delta_{iso} = \sigma_{ref} + m_{ref}\sigma_{iso}$ are: ^{25}Mg [σ_{ref} = 538.83 ppm, m_{ref} = −0.9533, standard deviation = 11.9 ppm][27]; ^{71}Ga [σ_{ref} = 1502.63 ppm, m_{ref} = −0.8667, rms error = 7.3 ppm][15]; ^{17}O [σ_{ref} = 223.70 ppm, m_{ref} = −0.8876, rms error = 12.1 ppm].[15] Standard deviations of the calculated data (computed over equivalent site coordination types in all y = 0.125 configurations) are denoted by σ_{sd}. [b] Gaussian distribution of the mean isotropic value $\overline{\delta_{iso}}$. [c] Root mean square P_Q obtained from the simulation of the disorder by using the Gaussian isotropic model. [d] Not applicable in the Gaussian isotropic model. [e] Not observed experimentally. [f] A more detailed breakdown for all oxygen sites can be found in Table S6.

quadrupolar broadening can be removed by two-dimensional (2D) multiple-quantum magic angle spinning (MQMAS)[53,54,75,76] leading to spectra (Figures 4b and S5b−S7b) that contain a signal from a single type of Mg site, but with a 2D line shape again indicating the presence of structural disorder. Second, and more importantly, the experimental mean isotropic chemical shift $\overline{\delta iso}$ is found at 21 ppm with a 2 ppm distribution (Tables 2 and S1), in keeping with a predominantly Mg^{VI} coordination.[21,47] This finding is consistent with the weak energetic preference for $Ga-V_O-Ga$ configurations disclosed by the DFT calculations discussed above and the previous static ^{25}Mg NMR spectra.[40]

The quadrupolar distribution associated with the structural disorder has been modeled by a Gaussian isotropic model[58−61] using an approach adopted for NMR of glasses and other disordered materials.[63,77,78] The method uses a probability density function (PDF) description of the strength (quadrupolar frequency ν_Q) and shape (asymmetry parameter η_Q) of the quadrupolar interaction tensor to characterize the MAS NMR line shape σ. The 2D MQMAS data and associated fitting of the Gaussian isotropic model line shape are presented in Figure 4b,c, from which a root-mean-square P_Q of 1−2 MHz is obtained (Tables 2 and S1), again in keeping with a disordered Mg^{VI} coordination.

The site-averaged theoretical ^{25}Mg CS and EFG tensors obtained from GIPAW calculations for the sixteen optimized $La_{16}Ga_{14}Mg_2O_{47}$ configurations (Tables 1 and S2) support the experimental values. In particular, the computed δ_{iso} of 16 ppm for Mg^{VI} is in good agreement with the experimental mean value of 21 ppm, bearing in mind the standard deviation of 2 ppm computed across all y = 0.125 configurations and the reference-related standard deviation of 11.9 ppm derived from a wide range of Mg oxyanions by Cahill et al.[27] The computed Mg^{VI} P_Q value (3.1 MHz) is marginally larger than the experimental range, although the difference falls within the combined range of the experimental error and theoretical deviation. The calculations also provide a δ_{iso} value for Mg^{V} of 38 ppm, lying some 22 ppm higher than that derived for Mg^{VI}.

In order to explore the likely limit of detection of a Mg^{V} resonance, spectral simulations were performed by using the DFT-derived NMR parameters for this site and by assuming structural disorder for static fields of 11.7 and 19.6 T (Figures S8−S10). The results suggest that a small but not insignificant amount (approximately 20−30% of all doped Mg cations) of Mg^{V} sites may be beyond the limit of detection under our experimental conditions.

3.2.2. ^{71}Ga. In light of the apparent prevalence of Mg^{VI} sites as discussed above, we now examine the ^{71}Ga NMR data for the $La_{1-x}Sr_xGa_{1-y}Mg_yO_{3-(x+y)/2}$ (x,y = 0.1−0.2) phases obtained under various experimental conditions. The static spectra (obtained at 20 T, Figure 5 and at multiple magnetic fields strengths, Figures S11−S12) are clearly dominated by a relatively narrow line that may be satisfactorily fitted[55,56] by an EFG tensor (Tables 2 and S3) with parameters that are consistent with Ga^{VI} coordination and very close to those derived from numerical simulation.[79,80] Stoichiometric $LaGaO_3$ was fit with a Gaussian line shape.[40] However, closer examination of the line shapes reveals the presence of at least one additional Ga resonance (see inserts in Figure 5 and Figures S11−S12) for all compounds except stoichiometric $LaGaO_3$. The additional resonance is much broader than that originating from the majority Ga^{VI} sites, with fitted C_Q = 8.3 ± 2.4 MHz (Tables 1 and S3) and δ_{iso} = 72 ± 22 ppm, the latter being extracted from the field dependence of the peak position (Figure S13). Such values are close to both the experimental[46] (δ_{iso} = 76 ± 10 ppm and C_Q = 15 ± 0.3 MHz) and theoretical[15] (δ_{iso} = 89.6 ppm and C_Q = 11.6 MHz) results obtained previously for the Ga^{V} site occurring in

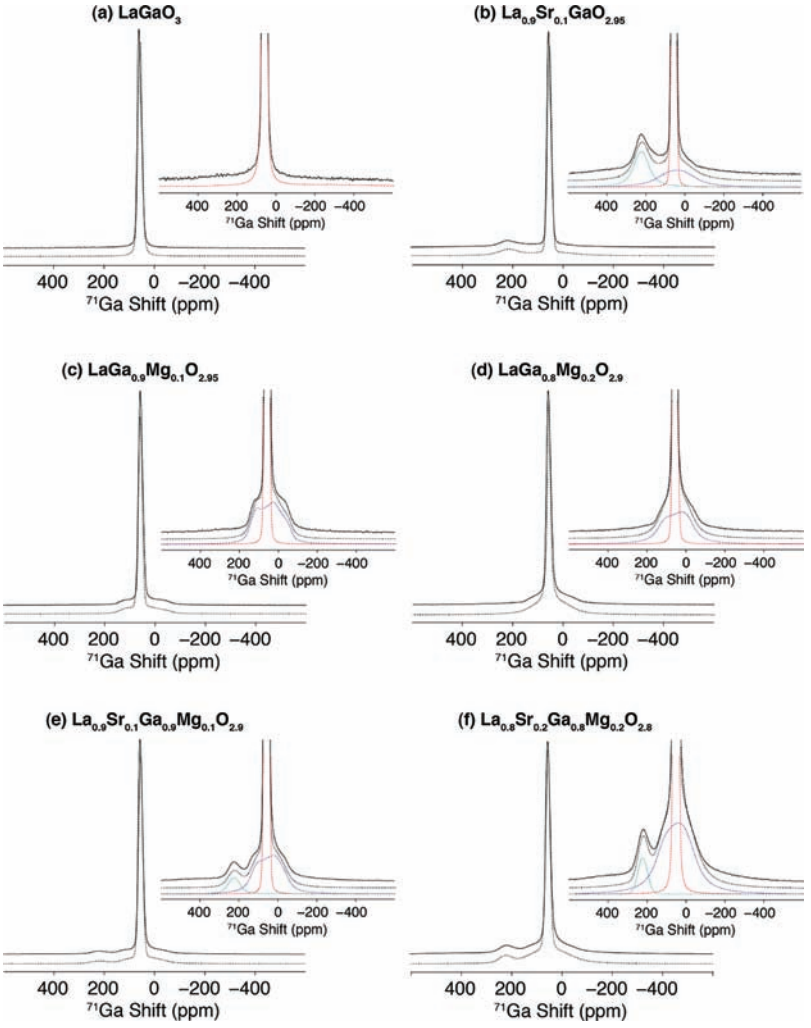

Figure 5. ^{71}Ga static NMR spectra of $La_{1-x}Sr_xGa_{1-y}Mg_yO_{3-(x+y)/2}$ (x,y = 0.1 − 0.2) obtained at 20 T. The insets show a magnified view highlighting the Ga^V sites. Experimental spectra are shown with full lines and best-fit simulations in black dashed lines. The individual site components are shown with dashed lines in red (Ga^{VI} in doped $LaGaO_3$), dark blue (Ga^{IV} in doped $LaGaO_3$), and light blue (Ga^{IV} in $LaSrGa_3O_7$) using the parameters given in Tables 2 and S3.

$LaGaGe_2O_7$, lending further support to the notion that the charge-balancing O vacancies introduced by Mg−doping occupy sites next to Ga cations. Finally, a third, weak environment was also observed in the static spectra of Sr-doped $LaGaO_3$, which was more clearly resolved under very fast MAS conditions at various fields (see Figures S14−S15). This resonance has a chemical shift of 227 ppm (Table 3 and Figure S13), which is in the chemical shift range expected for a tetrahedral Ga^{3+} ion; furthermore, it is only present in the Sr^{2+}-substituted materials. On this basis, the resonance is assigned to the Ga^{IV} sites present in the $LaSrGa_3O_7$ impurity phase commonly occurring in the preparation of the present doped materials (Figure S1).[9] The previously published ^{71}Ga static NMR spectra of $La_{1-x}Sr_xGa_{1-y}Mg_yO_{3-(x+y)/2}$ (x,y = 0.05−0.2) are close to ours (Figure 5) and were also fitted in a similar way with two sites with C_Q values of 1.3 and 7.8 MHz, but here both were assigned to Ga^{VI} sites and Ga^{VI} sites having oxygen vacancies beyond the nearest anion shell, respectively. These authors included a third component (with C_Q = 17 MHz) to the fit to account for an additional spectral feature that we were unable to detect in our spectra. This resonance was then assigned to five-fold coordinated Ga sites.

Examining the site-averaged Ga^{VI} GIPAW NMR parameters, the δ_{iso} value is in excellent agreement with experiment, but the C_Q parameter is overestimated (Tables 2 and S4). This is an interesting finding, given that our earlier GIPAW calculations of pure $LaGaO_3$ yield Ga^{VI} NMR parameters in excellent agreement with experiment,[15] the earlier computed values lying close to the experimental parameters presented here. Intuitively, it might be expected that the presence at ambient temperature of a relatively static distribution of dopants and vacancies in the second anion coordination shell of Ga^{VI} sites might lead to an increase in ^{71}Ga C_Q values, but the experimental spectra do not support this suggestion. It is possible that thermal motion, neglected in the present calculations, may play an important role in modifying C_Q and η_Q values, as suggested by our previous work.[15] A more likely suggestion is that the current analysis, which does not take into account the distribution of quadrupolar parameters, places a greater weight on the more symmetric environments that are located further from the substituents. The experimental and computed shifts of the Ga^V sites display significantly poorer agreement for reasons that are not entirely clear. Interestingly, our previous GIPAW calculations accurately

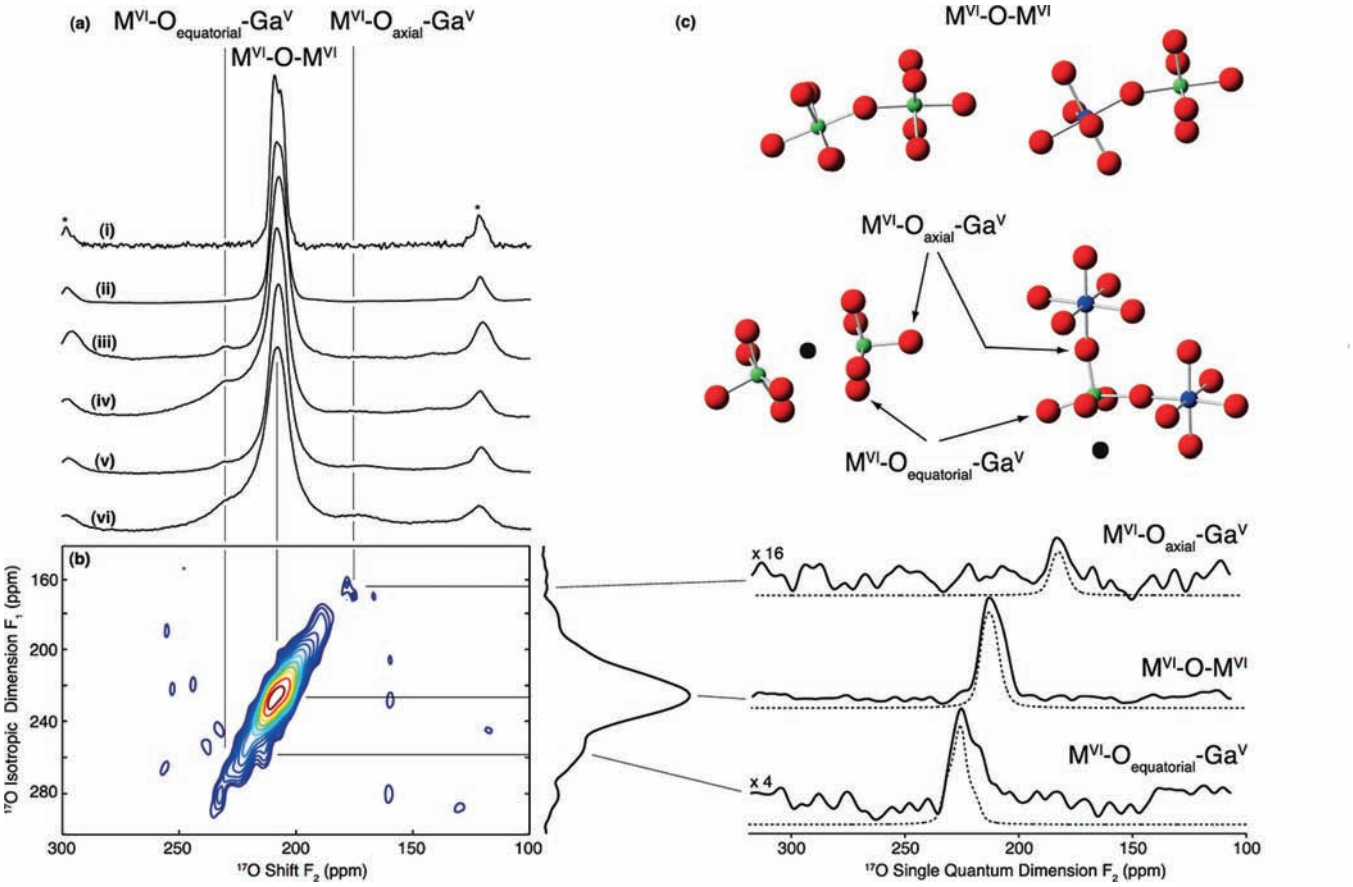

Figure 6. (a) ^{17}O MAS NMR spectrum of ^{17}O enriched $LaSr_{1-x}Ga_{1-y}Mg_yO_{3-(x+y/2}$ (x,y = 0.1−0.2) obtained at 19.6 T. One-dimensional spectra of (i) $LaGaO_3$, (ii) $La_{0.9}Sr_{0.1}GaO_{2.95}$, (iii) $LaGa_{0.9}Mg_{0.1}O_{2.95}$, (iv) $LaGa_{0.8}Mg_{0.2}O_{2.9}$, (v) $La_{0.1}Sr_{0.1}Ga_{0.1}Mg_{0.1}O_{2.9}$ and (vi) $La_{0.8}Sr_{0.2}Ga_{0.8}Mg_{0.2}O_{2.8}$. (b) Two-dimensional sheared ^{17}O triple-quantum (3Q) MAS spectrum of $La_{0.8}Sr_{0.2}Ga_{0.8}Mg_{0.2}O_{2.8}$. Right: isotropic projection of the 2D 3Q MAS. Cross sections (full lines) extracted parallel to F_2 of the 2D 3Q MAS spectrum at δ_1 of 180 (top), 232 (middle), and 245 (bottom) ppm along with the best fit simulation (dashed lines) using the parameters presented in Tables 2 and S5. (c) Representative optimized local structures showing the oxygen environments characteristic of $M^{VI}-O-M^{VI}$ and $M^{VI}-O_{ax/eq}-Ga^{V}$ (M = Ga or Mg) sites. Green, blue, and red spheres represent Ga, Mg, and O ions, respectively, while the black sphere denotes the oxygen vacancy, V_O.

reproduced the shift of the Ga^{V} site in $LaGaGe_2O_7$,[15] as discussed above, but it should be noted that the trigonal bipyramidal geometry of this site differs significantly from the distorted square pyramidal geometry (Figure 1b) produced by vacancy coordination in the present phases, so that we should not necessarily expect similar shifts. To the best of our knowledge, no oxide containing Ga^{V} in a square pyramidal geometry has been reported to date; therefore, we cannot pursue a strategy of obtaining and comparing Ga NMR spectra from a relevant model compound.

Summarizing the cation data, the direct experimental observation of resonances corresponding to Ga^{V}, Ga^{VI}, and Mg^{VI} environments indicate that, at ambient temperature, the compensatory O vacancies produced by Sr- and Mg-doping occur predominantly between Ga cations. The DFT-derived energetics presented above support this finding, although we note again that a small concentration of $Mg-V_O-Ga$ environments will likely be quenched into the y = 0.0625 and 0.125 phases prepared by rapid cooling from high temperature. Spectral simulations were performed to determine the minimum concentrations at which possible Mg^{V} environments might be resolved above the majority Mg^{VI} sites (Figures S8−S10). Combining the observed and simulated spectra, we suggest that O vacancies approach the large majority (greater than 70%) of Mg substituents no closer than to within their second anion coordination shells.

3.2.3. ^{17}O. ^{17}O (I = $^5/_2$) NMR spectra were collected to determine whether the anions themselves show any useful sensitivity to the distribution of dopant species and O vacancies. The ^{17}O MAS NMR spectrum of $LaGaO_3$ obtained at 19.6 T reveals only one O site at δ_{iso} = 223 ppm (Figures 6a and S16−S17, and Tables 2 and S5), which is assigned to O bridging two Ga^{VI} sites. Attempts by 2D MQMAS experiments (Figure S17) to resolve the two O sites anticipated in the orthorhombic *Pbnm* space group failed; this is ascribed to the fact that the chemical shifts of the two O sites are very similar, differing by only approximately 2.5 ppm in our previous GIPAW calculations.[15] While the dominant ^{17}O signal in the doped phases (i.e., $La_{1-x}Sr_xGa_{1-y}Mg_yO_{3-(x+y)/2}$ with x,y = 0.1−0.2) (Figures 6a and S18−S22) at δ_{iso} = 223 ppm is similar to that observed in the stoichiometric $LaGaO_3$ phase, an increase in the concentration of both Sr and Mg leads to the appearance of two new ^{17}O resonances at approximately 175 and 240 ppm (Figures 6a,b and S16). Importantly, we note that the intensities of these resonances correlate directly with the total concentration of both dopant species (i.e., $x + y$), rather than with the concentration of one of the species (i.e., either x or y). No apparent further sensitivity to the relative concentrations of the two dopant species was observed.

Note that these additional resonances could not be observed at low field (11.7 T) (Figure S16) and have thus not been in previous studies.[40]

Assignment of these resonances is non-trivial, and so we have examined the full set of ^{17}O GIPAW data for all y = 0.125 configurations to identify the O environments giving rise to the additional resonances. First, and somewhat surprisingly, the calculations reveal that the ^{17}O NMR parameters show little sensitivity to the identities of the cation species (i.e., Ga^{3+} or Mg^{2+}) coordinating with each O site (Table S6). For example, the mean δ_{iso} and C_Q values of the $Ga^{VI}-O-Ga^{VI}$ and $Ga^{VI}-O-Mg^{VI}$ environments differ by only 3.3 ppm and 1.66 MHz, respectively, indicating that the variations in the electronic structure at O sites are driven more by the proximity of the vacancies than by the nature of the coordinating cations. Thus, the dominant resonance assigned above to majority $Ga^{VI}-O-Ga^{VI}$ sites must be further broadened in scope to include all $M^{VI}-O-M^{VI}$ sites (M = Ga or Mg) irrespective of cation species. In contrast, cation substitution in some other perovskites has been shown to have a more significant effect on ^{17}O spectra. For example, the shifts of the $Sc^{III}-O-Zr^{IV}$ and $Zr^{IV}-O-Zr^{IV}$ environments in Sc-doped $BaZrO_3$ differ by approximately 20 ppm.[16] These differences in chemical shifts are nonetheless much smaller than those observed for changes of coordination number, bridging (essentially two-fold coordinate) three-, four-, and six-fold coordinate oxygen environments often varying by more than 100 ppm.[21,81]

Second and more importantly, the ^{17}O NMR spectra of the present phases exhibit a sensitivity to the presence of O vacancies that greatly exceeds the effects due to coordination with particular cation species. The GIPAW calculations support the experimental assignment of the dominant resonance at 223 ppm to majority $M^{VI}-O-M^{VI}$ sites, the corresponding mean computed shift being 221 ppm with a standard deviation of 7 ppm (Table 2). However, the resonances arising from O ions bonded to M^V cations are found to be significantly shifted relative to those for majority $M^{VI}-O-M^{VI}$ sites. The resonance shifted downfield by approximately 21 ppm (at δ_{iso} = 244 ppm) is found to correspond to O sites occupying equatorial (eq) positions with respect to the vacancy−cation axis (Figure 6c), while the resonance shifted upfield by approximately −44 ppm (at δ_{iso} = 182 ppm) corresponds to O sites occupying the axial (ax) positions (Figure 6c). The relative intensities of the two additional resonances are consistent with the proposed assignments. While we note that relative site occupancies obtained from the NMR spectra of quadrupolar nuclei[82] (such as ^{17}O) must be interpreted with care, a semi-quantitative intensity ratio of equatorial to axial oxygens of 4.5 ± 0.5 was obtained from spectral deconvolution of the ^{17}O NMR spectra (Figure 6), in good agreement with the anticipated intensity ratio of 4.

An examination of the set of optimized geometries provides some insight into the source of such disparate shifts. The Ga^V and Mg^V cations are each apparently repelled by the neighboring O vacancies, leading to a significant distortion away from the idealized square pyramidal M^V structure anticipated for coordination with an O vacancy (Figure 6c). More specifically, the Ga^V-O_{ax} bonds are on average approximately 0.08−0.09 Å shorter than the Ga^V-O_{eq} bonds, leading to the increased shielding of O_{ax} sites relative to O_{eq} observed in both the experimental and theoretical data. More broadly, this is consistent with findings in polyoxometallates[83] and carbonyl transition metals complexes,[84] where the positions of the O sites around a polyhedra were readily identifiable from their ^{17}O shifts. While the undercoordinated cations are almost exclusively Ga^V in the present phases, we note for completeness sake that an analogous trend emerges in the computed ^{17}O NMR parameters for O_{ax} and O_{eq} anions neighboring Mg^V sites, driven by a similar $Mg^V-O_{ax/eq}$ bond length difference of approximately 0.1 Å.

4. CONCLUSIONS

The present study demonstrates that an approach combining multinuclear NMR spectroscopy with first principles total energy and NMR calculations affords a comprehensive insight into the key defect chemistry underpinning the application of Sr- and Mg-doped $LaGaO_3$ as a next-generation SOFC electrolyte. The DFT energetics have been interpreted in terms of doping energies assuming a range of phase equilibria, and phase formation energies relative to the binary oxides, allowing for comparisons with previous interatomic potential and DFT calculations, and experimental calorimetry measurements. The ^{25}Mg and ^{71}Ga NMR experiments and DFT energetics all indicate that the O vacancies are located within the first anion coordination shell of the Ga species and do not approach the majority of the Mg dopants any closer than their second anion coordination shells. A key finding is that the strong $Mg-V_O$ binding inferred by previous computational and experimental studies is not observed here. Rather, there is a weak energetic preference for $Ga-V_O-Ga$ environments, although we anticipate the presence of significant concentrations of higher-energy $Mg-V_O-Ga$ environments if samples are quenched from high temperature. We have also identified and assigned distinct ^{17}O resonances arising from anions occupying equatorial and axial positions with respect to the Ga^V-V_O axis, the O chemical shifts showing an unexpected sensitivity to the distortions induced by nearby vacancies. We hope that this experimental and theoretical approach will find use to probe the effects of cation doping on local structure and anion dynamics in a broader range of electrolyte phases. Further NMR investigations of O exchange between the distinct local environments as a function of temperature and atmosphere within the notional operating range of the electrolyte are currently underway.

■ ASSOCIATED CONTENT

Supporting Information. Additional experimental details for the ^{71}Ga MAS spectra, additional discussion of the use of the Gaussian isotropic and Czjzek models to describe the distribution of quadrupolar parameters of the ^{25}Mg data, powder X-ray diffraction patterns of $La_{1-x}Sr_xGa_{1-y}Mg_yO_{3-(x+y)/2}$ (x,y = 0.1−0.2) (Figure S1), ^{25}Mg-enriched $La_{1-x}Sr_xGa_{1-y}Mg_yO_{3-(x+y)/2}$ (x,y = 0.1−0.2) (Figure S2), ^{17}O-enriched $La_{1-x}Sr_xGa_{1-y}Mg_yO_{3-(x+y)/2}$ (x,y = 0.1−0.2) (Figure S3), ^{25}Mg NMR spectra of ^{25}Mg-enriched $La_{1-x}Sr_xGa_{1-y}Mg_yO_{3-(x+y)/2}$ (x,y = 0.1−0.2) at 11.7 and 19.6 T (Figure S4), ^{25}Mg MQMAS NMR spectra of ^{25}Mg-enriched $La_{1-x}Sr_xGa_{1-y}Mg_yO_{3-(x+y)/2}$ (x,y = 0.1−0.2) at 19.6 T (Figures S5−S7), comparison of the experimental and simulated ^{25}Mg spectra of ^{25}Mg-enriched $La_{0.8}Sr_{0.2}Ga_{0.8}Mg_{0.2}O_{2.8}$ (Figure S8) at 19.6 T, Czjzek distribution simulation of ^{25}Mg spectra at 11.7 T (Figure S9) and 19.6 T (Figure S10), ^{71}Ga static NMR spectra of $La_{1-x}Sr_xGa_{1-y}Mg_yO_{3-(x+y)/2}$ (x,y = 0.1−0.2) at multiple magnetic fields (Figures S11−S12), plot of ^{71}Ga isotropic shift vs B_0^{-2} (Figure S13), ^{71}Ga MAS NMR spectra of $La_{1-x}Sr_xGa_{1-y}Mg_yO_{3-(x+y)/2}$ (x,y = 0.1−0.2) at 7 and 19.6 T (Figures S14−S15), ^{17}O NMR spectra of ^{17}O-enriched $La_{1-x}Sr_xGa_{1-y}Mg_yO_{3-(x+y)/2}$ (x,y = 0.1−0.2) at 11.7 and 19.6 T (Figure S16), ^{17}O MQMAS NMR spectra of ^{17}O enriched $La_{1-x}Sr_xGa_{1-y}Mg_yO_{3-(x+y)/2}$ (x,y = 0.1−0.2) at 19.6 T

(Figures S17−S22), experimental (Table S1) and calculated (Table S2) ^{25}Mg NMR parameters, experimental (Table S3) and calculated (Table S4) ^{71}Ga NMR parameters, experimental (Table S5) and calculated (Table S6) ^{17}O NMR parameters, optimized structures and complete GIPAW NMR data for all configurations considered. This material is available free of charge via the Internet at http://pubs.acs.org.

AUTHOR INFORMATION

Corresponding Author
cpg27@cam.ac.uk

ACKNOWLEDGMENT

We thank Dr. Thomas F. Kemp (University of Warwick, U.K.) and Dr. Jacco D. van Beek (ETH Zurich, Switzerland) for useful discussions. F.B. and C.P.G. acknowledge the support of the NSF via Grant DMR0804737, and D.S.M. and C.P.G. the NSF via Grant CHE0714183. F.B. also thanks the French Foreign Office for a post-doctoral Lavoisier fellowship 2007−2008 (Grant 530227G). The UK 850 MHz solid-state NMR Facility used in part of this research was funded by EPSRC and BBSRC, as well as the University of Warwick including partial funding through Birmingham Science City Advanced Materials Projects 1 and 2 supported by Advantage West Midlands (AWM) and the European Regional Development Fund (ERDF). An allocation of time upon the NANO computer cluster at the Centre for Functional Nanomaterials, Brookhaven National Laboratory, U.S.A., which is supported by the U.S. Department of Energy, Office of Basic Energy Sciences, under Contract No. DE-AC02-98CH10886 is also acknowledged. Part of this work is sponsored by the National High Magnetic Field Laboratory through National Science Foundation Cooperative Agreement DMR0654118 and by the State of Florida.

REFERENCES

(1) Ishihara, T.; Kudo, T.; Matsuda, H.; Takita, Y. *J. Am. Ceram. Soc.* **1994**, *77*, 1682.
(2) Ishihara, T.; Matsuda, H.; Takita, Y. *J. Am. Chem. Soc.* **1994**, *116*, 3801.
(3) Feng, M.; Goodenough, J. B.; Huang, K. Q.; Milliken, C. *J. Power Sources* **1996**, *63*, 47.
(4) Huang, K.; Tichy, R.; Goodenough, J. B.; Milliken, C. *J. Am. Ceram. Soc.* **1998**, *81*, 2581.
(5) Huang, K.; Tichy, R. S.; Goodenough, J. B. *J. Am. Ceram. Soc.* **1998**, *81*, 2565.
(6) Huang, K.; Tichy, R. S.; Goodenough, J. B. *J. Am. Ceram. Soc.* **1998**, *81*, 2576.
(7) Lybye, D.; Poulsen, F. W.; Mogensen, M. *Solid State Ionics* **2000**, *128*, 91.
(8) Nguyen, T. L.; Dokiya, M.; Wang, S.; Tagawa, H.; Hashimoto, T. *Solid State Ionics* **2000**, *130*, 229.
(9) Chen, T. Y.; Fung, K.-Z. *J. Alloys Compd.* **2004**, *368*, 106.
(10) Slater, P. R.; Irvine, J. T. S.; Ishihara, T.; Takita, Y. *J. Solid State Chem.* **1998**, *139*, 135.
(11) Kim, N.; Grey, C. P. *Science* **2002**, *297*, 1317.
(12) Holmes, L.; Peng, L.; Heinmaa, I.; O'Dell, L. A.; Smith, M. E.; Vannier, R.-N.; Grey, C. P. *Chem. Mater.* **2008**, *20*, 3638.
(13) Blanc, F.; Middlemiss, D. S.; Gan, Z.; Grey, C. P. Materials Research Society Fall Meeting, Boston, MA, December 1−5, 2008.
(14) Middlemiss, D. S.; Blanc, F.; Grey, C. P. *ECS Trans.* **2009**, *25*, 1709.
(15) Middlemiss, D. S.; Blanc, F.; Pickard, C. J.; Grey, C. P. *J. Magn. Reson.* **2010**, *204*, 1.
(16) Buannic, L.; Blanc, F.; Hung, I.; Gan, Z.; Grey, C. P. *J. Mater. Chem.* **2010**, *20*, 6322.
(17) Adler, S. B.; Reimer, J. A. *Solid State Ionics* **1996**, *91*, 175.
(18) Adler, S. B.; Smith, J. W.; Reimer, J. A. *J. Chem. Phys.* **1993**, *98*, 7613.
(19) Kim, N.; Stebbins, J. F. *Chem. Mater.* **2007**, *19*, 5742.
(20) Huang, H.; Hsieh, C.-H.; Kim, N.; Stebbins, J.; Pninz, F. *Solid State Ionics* **2008**, *179*, 1442.
(21) MacKenzie, K. J. D.; Smith, M. E. *Multinuclear Solid-State NMR of Inorganic Materials*; Elsevier: Oxford, 2002; Vol. 6.
(22) Clark, S. J.; Segall, M. D.; Pickard, C. J.; Hasnip, P. J.; Probert, M. J.; Refson, K.; Payne, M. C. *Z. Kristallogr.* **2005**, *220*, 567.
(23) Pickard, C. J.; Mauri, F. *Phys. Rev. B* **2001**, 63.
(24) Yates, J. R.; Pickard, C. J.; Mauri, F. *Phys. Rev. B* **2007**, 76.
(25) Pourpoint, F.; Gervais, C.; Bonhomme-Coury, L.; Azaïs, T.; Coelho, C.; Mauri, F.; Alonso, B.; Babonneau, F.; Bonhomme, C. *Appl. Magn. Reson.* **2007**, *32*, 435.
(26) Pourpoint, F.; Kolassiba, A.; Gervais, C.; Azaïs, T.; Bonhomme-Coury, L.; Bonhomme, C.; Mauri, F. *Chem. Mater.* **2007**, *19*, 6367.
(27) Cahill, L. S.; Hanna, J. V.; Wong, A.; Freitas, J. C. C.; Yates, J. R.; Harris, R. K.; Smith, M. E. *Chem.—Eur. J.* **2009**, *15*, 9785.
(28) Reader, S. W.; Mitchell, M. R.; Johnston, K. E.; Pickard, C. J.; Whittle, K. R.; Ashbrook, S. E. *J. Phys. Chem. C* **2009**, *113*, 18874.
(29) Zurek, E.; Autschbach, J. *Int. J. Quantum Chem.* **2009**, *109*, 3343.
(30) Kim, J.; Middlemiss, D. S.; Chernova, N. A.; Zhu, B. Y. X.; Masquelier, C.; Grey, C. P. *J. Am. Chem. Soc.* **2010**, *132*, 16825.
(31) Johnston, K. E.; Tang, C. C.; Parker, J. E.; Knight, K. S.; Lightfoot, P.; Ashbrook, S. E. *J. Am. Chem. Soc.* **2010**, *132*, 8732.
(32) Webber, A. L.; Emsley, L.; Claramunt, R. M.; Brown, S. P. *J. Phys. Chem. A* **2010**, *114*, 10435.
(33) Widdifield, C. M.; Bryce, D. L. *J. Phys. Chem. A* **2010**, *114*, 10810.
(34) Mitchell, M. R.; Reader, S. W.; Johnston, K. E.; Pickard, C. J.; Whittle, K. R.; Ashbrook, S. E. *Phys. Chem. Chem. Phys.* **2011**, *13*, 488.
(35) Johnston, K. E.; Griffin, J. M.; Walton, R. I.; Dawson, D. M.; Lightfoot, P.; Ashbrook, S. E. *Phys. Chem. Chem. Phys.* **2011**, *13*, 7565.
(36) Hanna, J. V.; Pike, K. J.; Charpentier, T.; Kemp, T. F.; Smith, M. E.; Lucier, B. E. G.; Schurko, R. W.; Cahill, L. S. *Chem.—Eur. J.* **2010**, *16*, 3222.
(37) Special issue on GIPAW NMR calculations. *Magn. Reson. Chem.* **2010**, *48*, S1−S175.
(38) Martineau, C.; Fayon, F.; Suchomel, M. R.; Allix, M.; Massiot, D.; Taulelle, F. *Inorg. Chem.* **2011**, *50*, 2644.
(39) Charpentier, T. *Solid State Nucl. Magn. Reson.* **2011**, *40*, 1.
(40) Buzlukov, A.; Trokiner, A.; Kozhevnikov, V.; Verkhovskii, S.; Yakubovsky, A.; Leonidov, I.; Gerashenko, A.; Stepanov, A.; Baklanova, I.; Tankeyev, A. *J. Solid State Chem.* **2011**, *184*, 36.
(41) Stebbins, J. F.; Kroeker, S.; Andrault, D. *Geophys. Res. Lett.* **2001**, *28*, 615.
(42) Stebbins, J. F.; Kojitani, H.; Akaogi, M.; Navrotsky, A. *Am. Mineral.* **2003**, *88*, 1161.
(43) Oikawa, I.; Ando, M.; Noda, Y.; Amezawa, K.; Kiyono, H.; Shimizu, T.; Tansho, M.; Maekawa, H. *Solid State Ionics* **2011**, *192*, 83.
(44) Bradley, S. M.; Howe, R. F.; Kydd, R. A. *Magn. Reson. Chem.* **1993**, *31*, 883.
(45) Stebbins, J. F. In *Handbook of Physical Constants*; Ahrens, T. J., Ed.; American Geophysical Union: Washington D.C., 1995; p 303.
(46) Massiot, D.; Vosegaard, T.; Magneron, N.; Trumeau, D.; Montouillout, V.; Berthet, P.; Loiseau, T.; Bujoli, B. *Solid State Nucl. Magn. Reson.* **1999**, *15*, 159.
(47) Mackenzie, K. J. D.; Meinhold, R. H. *Am. Mineral.* **1994**, *79*, 250.
(48) Khan, M. S.; Islam, M. S.; Bates, D. R. *J. Phys. Chem. B* **1998**, *102*, 3099.
(49) Islam, M. S.; Davies, R. A. *J. Mater. Chem.* **2004**, *14*, 86.
(50) Haavik, C.; Ottesen, E. M.; Nomura, K.; Kilner, J. A.; Norby, T. *Solid State Ionics* **2004**, *174*, 233.
(51) Ishihara, T.; Matsuda, H.; Takita, Y. *Solid State Ionics* **1995**, *79*, 147.

(52) Frydman, L. In *Encyclopedia of Nuclear Magnetic Resonance*; Grant, D. M. and Harris, R. K., Eds.; John Wiley & Sons: Chichester, 2002; Vol. 9, p 262.
(53) Gan, Z.; Kwak, H.-T. *J. Magn. Reson.* **2004**, *168*, 346.
(54) Gan, Z.; Gor'kov, P. L.; Brey, W. W.; Sideris, P. J.; Grey, C. P. *J. Magn. Reson.* **2009**, *200*, 2.
(55) van Beek, J. D. *J. Magn. Reson.* **2007**, *187*, 19.
(56) Bak, M.; Rasmussen, J. T.; Nielsen, N. C. *J. Magn. Reson.* **2000**, *147*, 296.
(57) Hodgkinson, P.; Emsley, L. *Prog. Nucl. Magn. Reson. Spectrosc.* **2000**, *36*, 201.
(58) Le Caër, G.; Brand, R. A. *J. Phys.: Condens. Matter* **1998**, *10*, 10715.
(59) d'Espinose de Lacaillerie, J.-B.; Fretigny, C.; Massiot, D. *J. Magn. Reson.* **2008**, *192*, 244.
(60) Le Caër, G.; Bureau, B.; Massiot, D. *J. Phys.: Condens. Matter* **2010**, 22.
(61) Czjzek, G.; Fink, J.; Götz, F.; Schmidt, H.; Coey, J. M. D.; Rebouillat, J. P.; Liénard, A. *Phys. Rev. B* **1981**, *23*, 2513.
(62) Massiot, D.; Fayon, F.; Capron, M.; King, I.; Le Calvé, S.; Alonso, B.; Durand, J.-O.; Bujoli, B.; Gan, Z.; Hoatson, G. *Magn. Reson. Chem.* **2002**, *40*, 70.
(63) Neuville, D. R.; Cormier, L.; Massiot, D. *Geochim. Cosmochim. Acta* **2004**, *68*, 5071.
(64) Kemp, T. F.; Smith, M. E. *Solid State Nucl. Magn. Reson.* **2009**, *35*, 252.
(65) Profeta, M.; Mauri, F.; Pickard, C. J. *J. Am. Chem. Soc.* **2003**, *125*, 541.
(66) Pyykkö, P. *Mol. Phys.* **2001**, *99*, 1617.
(67) Perdew, J. P.; Burke, K.; Ernzerhof, M. *Phys. Rev. Lett.* **1996**, *77*, 3865.
(68) Kajitani, M.; Matsuda, M.; Hoshikawa, A.; Harjo, S.; Kamiyama, T.; Ishigaki, T.; Izumi, F.; Miyake, M. *Chem. Mater.* **2005**, *17*, 4235.
(69) Kuwabara, A.; Tanaka, I. *J. Phys. Chem. B.* **2004**, *108*, 9168.
(70) Kanke, Y.; Navrotsky, A. *J. Solid State Chem.* **1998**, *141*, 424.
(71) Kuncewicz-Kupczyk, W.; Kobertz, D.; Miller, M.; Chatillon, C.; Singheiser, L.; Hilpert, K. *J. Am. Ceram. Soc.* **2002**, *85*, 2299.
(72) Cheng, J.; Navrotsky, A. *J. Solid State Chem.* **2004**, *177*, 126.
(73) Calle-Vallejo, F.; Martinez, J. I.; García-Lastra, J. M.; Mogensen, M.; Rossmeisl, J. *Angew. Chem., Int. Ed.* **2010**, *49*, 7699.
(74) Jager, C.; Kunath, G.; Losso, P.; Scheler, G. *Solid State Nucl. Magn. Reson.* **1993**, *2*, 73.
(75) Frydman, L.; Harwood, J. S. *J. Am. Chem. Soc.* **1995**, *117*, 5367.
(76) Medek, A.; Harwood, J. S.; Frydman, L. *J. Am. Chem. Soc.* **1995**, *117*, 12779.
(77) Hoatson, G. L.; Zhou, D. H.; Fayon, F.; Massiot, D.; Vold, R. L. *Phys. Rev. B* **2002**, *66*.
(78) Keppert, M.; Rakhmatullin, A.; Simko, F.; Deschamps, M.; Haarberg, G. M.; Bessada, C. *Magn. Reson. Chem.* **2008**, *46*, 803.
(79) Bastow, T. J.; Mathews, T.; Sellar, J. R. *Solid State Ionics* **2004**, *175*, 129.
(80) Ash, J. T.; Grandinetti, P. J. *Magn. Reson. Chem.* **2006**, *44*, 823.
(81) Ashbrook, S. E.; Smith, M. E. *Chem. Soc. Rev.* **2006**, *35*, 718.
(82) Massiot, D.; Bessada, C.; Coutures, J. P.; Taulelle, F. *J. Magn. Reson.* **1990**, *90*, 231.
(83) Filowitz, M.; Ho, R. K. C.; Klemperer, W. G.; Shum, W. *Inorg. Chem.* **1979**, *18*, 93.
(84) Salzmann, R.; Kaupp, M.; McMahon, M. T.; Oldfield, E. *J. Am. Chem. Soc.* **1998**, *120*, 4771.